2. THE PAYLOAD: OVERVIEW AND OPTICAL ELEMENTS

This chapter gives an overview of the Hipparcos payload with particular reference to the optical elements. Images of stars from the two fields of view were brought together by the 'beam-combining mirror', the spherical mirror, and the flat folding mirror, to a focal surface where the modulating grid was located. Manufactured on the same substrate, the 'main grid' consisted of 2688 parallel slits, with a projected spacing of 1.208 arcsec and covering a field of $0\overset{\circ}{.}9 \times 0\overset{\circ}{.}9$*, and the 'star mapper grids' each consisting of two sets of four slits (vertical and chevron). Modulated signals from the main grid represented the basic primary mission data, while the modulated signals from the star mapper grid yielded information on the three-axis attitude of the satellite. Light coming through the main grid was transferred to the image dissector tube detector by the main detector relay lens assembly, and light modulated by the star mapper grid was 'picked off' by a 45° prism and transferred to the photomultiplier (star mapper) detectors by the star mapper relay lens assembly. A 'chromaticity filter' could be inserted into the parallel beam to provide in-orbit measurements of the telescope's chromatic aberration.*

2.1. Introduction

The Hipparcos payload was built around an all-reflective Schmidt telescope, working in the visible part of the electromagnetic spectrum. It had an entrance pupil of 290 mm diameter and a focal length of 1400 mm. A modulating grid was located at the telescope's focal surface, consisting of 2688 parallel slits with a period of 1.208 arcsec, and covering a square field of about $0\overset{\circ}{.}9 \times 0\overset{\circ}{.}9$.

The modulating grid was re-imaged onto the photocathode of an image dissector tube by means of a set of folding mirrors and relay lenses, constituting the image dissector tube relay optics. Two image dissector tube detectors and two sets of relay optics were used in cold redundancy (i.e. the redundant detector was switched off when not in use), the selection being performed by means of a switching mirror.

The instantaneous field of view of each image dissector tube was nominally circular, with a diameter of about 38 arcsec. It could be directed to any point of the $0\overset{\circ}{.}9 \times 0\overset{\circ}{.}9$ field by varying the currents applied to the deflection coils.

Table 2.1. Payload characteristics.

Optics:	Telescope configuration	All-reflective Schmidt
	Field of view	$0\overset{\circ}{.}9 \times 0\overset{\circ}{.}9$
	Separation between fields	58°
	Diameter of primary mirror	290 mm
	Focal length	1400 mm
	Scale at focal surface	6.8μm per arcsec
	Mirror surface accuracy	$\lambda/60$ rms (at $\lambda = 550$ nm)
Primary Detection System:	Modulating grid	2688 slits
	Slit period	1.208 arcsec (8.2μm)
	Detector	Image dissector tube
	Photocathode	S20
	Scale at photocathode	3.0μm per arcsec
	Sensitive field of view	38 arcsec diameter
	Spectral range	375–750 nm
	Sampling frequency	1200 Hz
Star Mapper (Tycho) System:	Modulating grid	4 slits perpendicular to scan 4 slits at ±45° inclination
	Detectors	Photomultiplier tubes
	Photocathode	Bi-alkali
	Spectral range (B_T)	$\lambda_{\mathrm{eff}} = 430$ nm, $\Delta\lambda = 90$ nm
	Spectral range (V_T)	$\lambda_{\mathrm{eff}} = 530$ nm, $\Delta\lambda = 100$ nm
	Sampling frequency	600 Hz

In addition to the primary detection chain (consisting of the modulating grid and the image dissector tube), the payload included two star mappers which were also used in cold redundancy. The primary function of the star mapper was to provide data allowing the on-board three-axis satellite attitude determination (a task performed by the on-board computer) and the *a posteriori* determination of the attitude (a task performed by the data analysis consortia on the ground).

Each star mapper consisted of a star mapper grid, located at one side of the main modulating grid, and two photomultipliers, measuring the light transmitted by the whole star mapper grid in two different spectral bands—B_T and V_T. The spectral separation was accomplished by means of a dichroic beam splitter, which reflected the shorter wavelength light (the B_T band) onto one photomultiplier and transmitted the longer wavelength light (the V_T band) onto the other.

Table 2.1 provides a summary of some of the key features of the payload. Tables 2.2–2.4 give a summary of the transmission of the various elements comprising the Hipparcos payload, both for the primary detection chain, and for the Tycho B_T and V_T chains, respectively. These figures are based on measurements at unit level during the on-ground calibrations.

Table 2.2. Spectral transmittance/quantum efficiency (QE) of the main detection chain, taking into account all payload elements (predicted performance at the start of the mission based on ground calibrations).

λ (nm)	Beam Combiner	Mirrors	Grid Substrate	Relay Optics	Detector	Total QE*
350	0.86	0.74	0.73	0.16	0.02	0.002
375	0.85	0.72	0.82	0.56	0.03	0.009
400	0.95	0.90	0.91	0.79	0.04	0.027
425	0.96	0.92	0.92	0.81	0.06	0.042
450	0.97	0.94	0.93	0.83	0.08	0.058
475	0.97	0.94	0.94	0.85	0.08	0.060
500	0.97	0.94	0.94	0.88	0.07	0.055
525	0.97	0.94	0.94	0.90	0.06	0.050
550	0.97	0.94	0.94	0.91	0.05	0.044
575	0.97	0.94	0.94	0.92	0.05	0.038
600	0.97	0.95	0.94	0.91	0.04	0.033
625	0.97	0.95	0.94	0.90	0.04	0.027
650	0.97	0.95	0.94	0.84	0.03	0.022
675	0.97	0.95	0.93	0.78	0.03	0.018
700	0.97	0.95	0.93	0.72	0.02	0.014
725	0.97	0.95	0.93	0.65	0.02	0.010
750	0.97	0.95	0.92	0.58	0.01	0.008
775	0.97	0.95	0.91	0.52	0.01	0.005
800	0.97	0.95	0.90	0.45	0.01	0.004
825	0.97	0.95	0.90	0.40	0.01	0.002

[*] In determining the average count rate from a star, the total efficiency given is further affected by the opaque parts of the modulating grid. This factor is nominally given by the ratio of the slit width to the grid period, or $3.13/8.20 \simeq 0.38$ (Table 2.5), but in reality it is further reduced by diffraction. The absolute detection efficiency, of about 10^{-2}, takes this into account.

2.2. Payload Configuration and Layout

The overall payload configuration is shown in Figure 2.1. The payload functional diagram is shown in Figure 2.2 and the payload electrical block diagram in Figure 2.3. The payload consisted of four main assemblies (see Figure 2.4):

(a) the two baffle assemblies: two external baffles protected the telescope assembly from stray light. They were mounted separately on the spacecraft upper platform, with no mechanical link with the other assemblies of the payload, except for the overlapping multi-layer insulation;

(b) the telescope assembly: this included all elements between the two optical entrance apertures and the grid unit: the three telescope mirrors and all associated structural elements necessary to maintain them at their nominal positions. All hardware associated with the thermal control (the multi-layer insulation, heaters, and thermistors) rested on separate structural elements. The telescope assembly also ensured the mechanical and thermal conductive interfaces with the spacecraft. An isostatic mounting of the payload onto the spacecraft employed three titanium bipods;

Table 2.3. Spectral transmittance/quantum efficiency (QE) of the B_T star mapper detection chain (vertical slits) taking into account all payload elements. The table gives the predicted performance at the beginning of the mission based on ground calibrations, i.e. without transmission degradation due to irradiation effects.

λ (nm)	Beam Combiner	Mirrors	Grid	Dichroic	Relay Optics	Diffraction Loss	Detector QE	Total QE
350	0.86	0.72	0.83	0.01	0.87	0.865	0.15	0.001
375	0.85	0.63	0.88	0.50	0.92	0.815	0.18	0.032
400	0.95	0.86	0.90	0.85	0.93	0.785	0.20	0.091
425	0.96	0.92	0.91	0.92	0.93	0.760	0.20	0.105
450	0.97	0.93	0.92	0.80	0.93	0.735	0.20	0.091
475	0.97	0.93	0.92	0.20	0.93	0.720	0.17	0.019
500	0.97	0.93	0.92	0.04	0.93	0.700	0.15	0.004
525	0.97	0.93	0.92	0.00	0.93	0.690	0.14	0.000
550	0.97	0.93	0.92	0.00	0.94	0.680	0.11	0.000
575	0.97	0.93	0.92	0.00	0.94	0.670	0.07	0.000
600	0.97	0.93	0.91	0.00	0.94	0.660	0.04	0.000
625	0.97	0.93	0.90	0.01	0.92	0.655	0.02	0.000
650	0.97	0.93	0.88	0.03	0.89	0.650	0.01	0.000
675	0.97	0.93	0.87	0.03	0.85	0.645	0.00	0.000
700	0.97	0.94	0.85	0.02	0.80	0.640	0.00	0.000
725	0.97	0.94	0.84	0.03	0.76	0.635	0.00	0.000
750	0.97	0.94	0.83	0.03	0.70	0.630	0.00	0.000
775	0.97	0.95	0.81	0.03	0.65	0.625	0.00	0.000

Table 2.4. Spectral transmittance/quantum efficiency (QE) of the V_T star mapper detection chain (vertical slits) taking into account all payload elements. The table gives the predicted performance at the beginning of the mission based on ground calibrations, i.e. without transmission degradation due to irradiation effects.

λ (nm)	Beam Combiner	Mirrors	Grid	Dichroic	Relay Optics	Diffraction Loss	Detector QE	Total QE
350	0.86	0.71	0.83	0.00	0.70	0.865	0.15	0.000
375	0.85	0.63	0.88	0.00	0.66	0.815	0.17	0.000
400	0.95	0.86	0.90	0.00	0.83	0.785	0.19	0.000
425	0.96	0.92	0.91	0.00	0.85	0.760	0.19	0.000
450	0.97	0.93	0.92	0.00	0.86	0.735	0.19	0.000
475	0.97	0.93	0.92	0.38	0.87	0.720	0.17	0.008
500	0.97	0.93	0.93	0.85	0.88	0.700	0.16	0.068
525	0.97	0.93	0.92	0.95	0.88	0.690	0.14	0.068
550	0.97	0.93	0.92	0.94	0.89	0.680	0.12	0.058
575	0.97	0.93	0.91	0.95	0.89	0.670	0.08	0.038
600	0.97	0.93	0.90	0.97	0.89	0.660	0.04	0.017
625	0.97	0.93	0.88	0.96	0.88	0.655	0.02	0.009
650	0.97	0.93	0.87	0.95	0.85	0.650	0.01	0.003
675	0.97	0.93	0.85	0.94	0.81	0.645	0.00	0.001
700	0.97	0.94	0.85	0.93	0.76	0.640	0.00	0.000
725	0.97	0.94	0.84	0.93	0.72	0.635	0.00	0.000
750	0.97	0.94	0.83	0.93	0.67	0.630	0.00	0.000
775	0.97	0.95	0.81	0.92	0.63	0.625	0.00	0.000

Colour figure to be inserted here

Figure 2.1. *Overview of the payload. Light entered from the two baffles (shown red and blue) and fell onto the beam-combining mirror, where it was brought to a common focus where the modulating grids were located (top). In the bottom figure, the path of the light reaching the (main) image dissector tube detector is shown as a red-dashed line, while the light reaching the star mapper detector is shown in blue. A dichroic filter split the latter into the* B_T *and* V_T *channels, which were detected separately.*

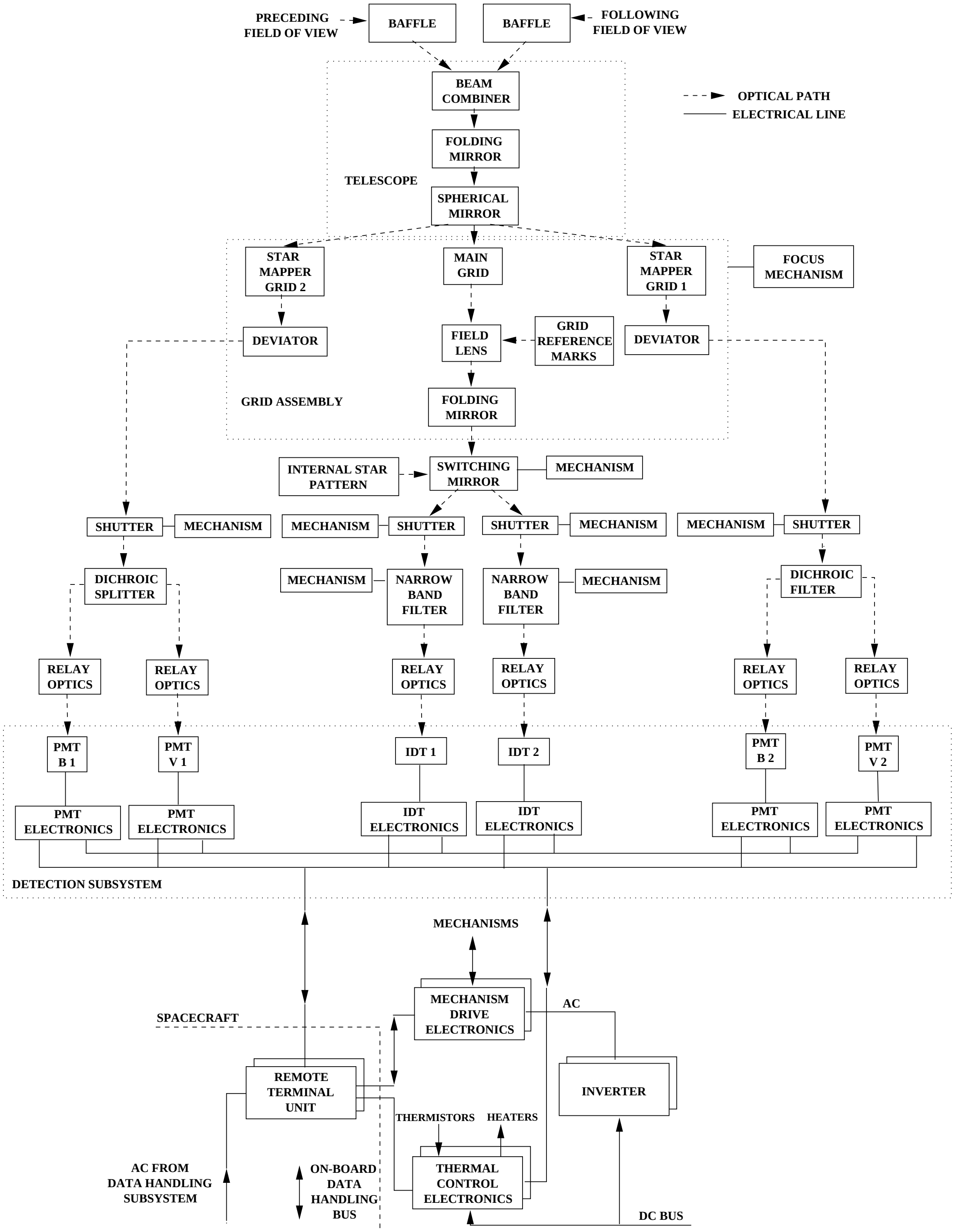

Figure 2.2. *Payload functional diagram, illustrating the path of the light through the payload, along with the corresponding shutters, mechanisms, and detectors associated with the (main) image dissector tube detectors (IDT) and the star mapper photomultiplier tubes (PMT). Redundant systems (indicated 1/2) were provided in all paths, eliminating single-point failures in the payload.*

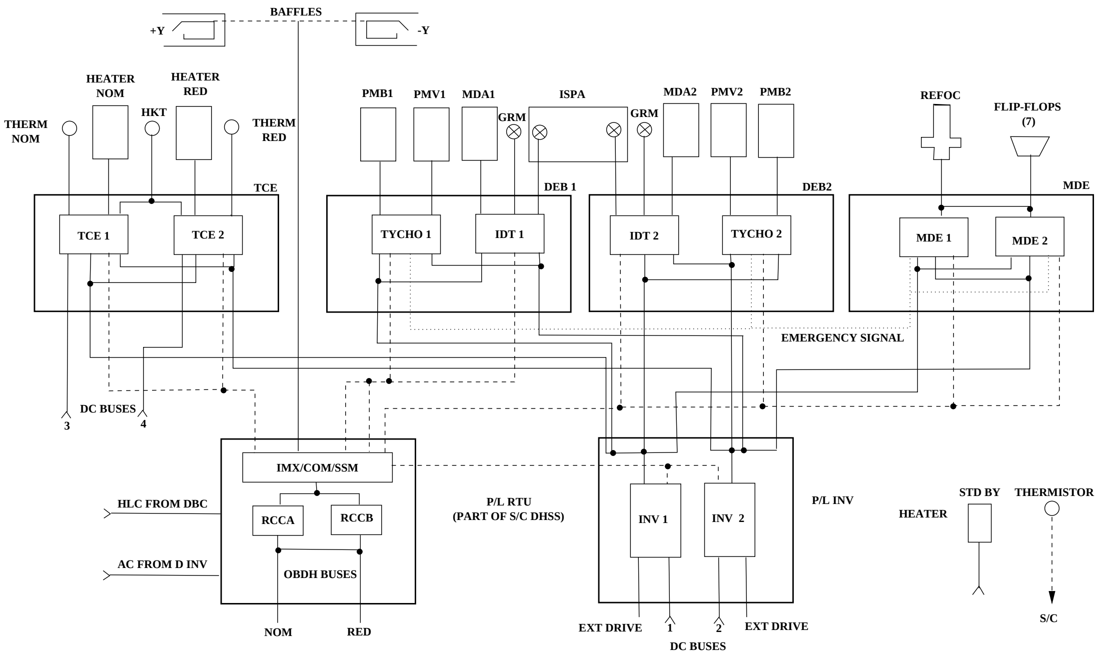

Figure 2.3. *Payload electrical block diagram. Heaters and thermistors were associated with each of the redundant thermal control electronics (TCE). DEB: detection electronics box; GRM: grid reference marks; IDT: image dissector tube; INV: invertor; MDE: mechanism drive electronics; OBDH: on-board data handling; RTU: remote terminal unit; PM: photomultiplier (star mapper).*

(c) the focal-plane assembly: this included all elements from the grid to the image dissector tube and photomultiplier detectors. The focal-plane assembly was mechanically attached to the telescope assembly. It consisted of a rectangular platform supporting all the equipment required to transform the optical signals produced by the telescope assembly into electrical digital signals. The main components of the focal-plane assembly were: the refocusing assembly comprising the main grid, the star mapper grids, and the focus mechanism; the relay optics, filters, and mirrors, required to relay the photons from the grid to the detectors; the detectors (image dissector tubes and photomultipliers); the detection electronics; the mechanisms (shutters, switching mirror, etc.); and an internal star pattern assembly used for calibration purposes;

(d) the service electronics units, consisted of the payload inverter, the thermal-control electronics, and the mechanism drive electronics. Functionally, these three units were complemented by the remote terminal unit (not strictly part of the payload items). These boxes were installed on the upper platform of the spacecraft and had no mechanical link with the rest of the payload, except for the electrical cables.

The payload main assembly was a higher-level assembly, consisting of the telescope assembly and the focal-plane assembly, as illustrated in Figure 2.5. The payload main assembly was a single physical box after integration of the focal-plane assembly onto the telescope assembly.

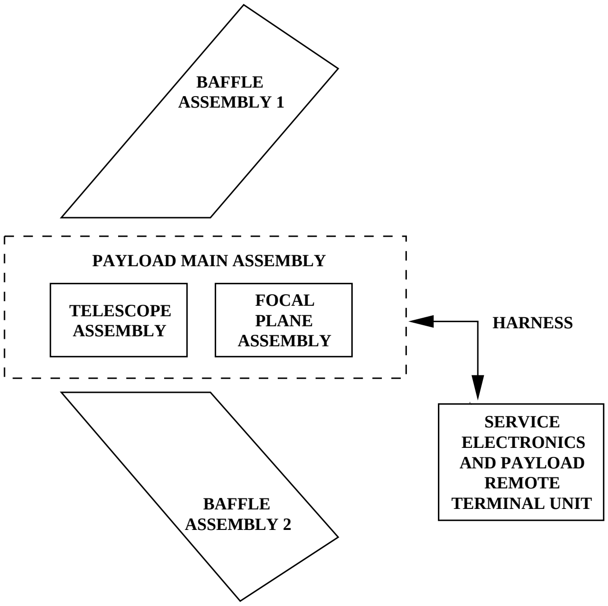

Figure 2.4. *Breakdown of the payload hardware at assembly level.*

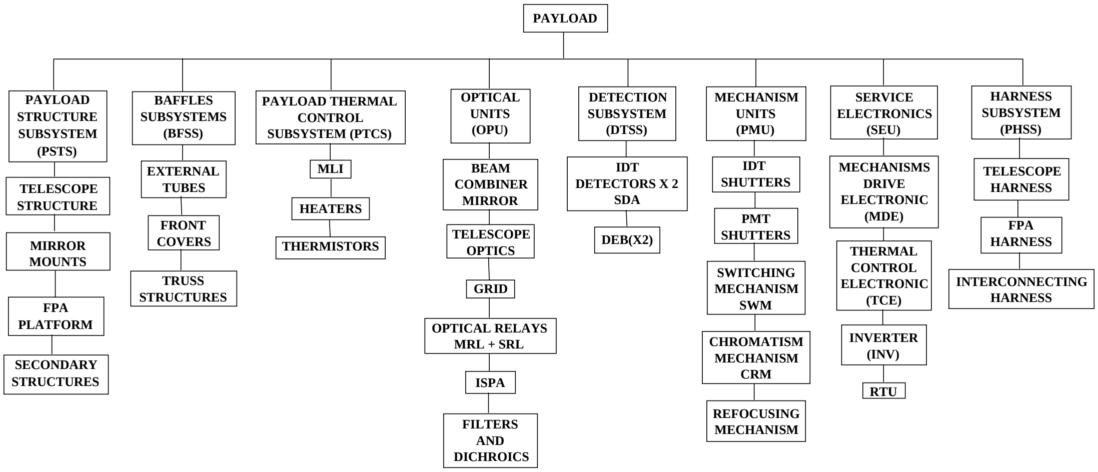

Figure 2.5. *Breakdown of the payload hardware at subsystem level (DEB: detection electronics box; FPA: focal plane assembly; IDT: image dissector tube; ISPA: internal star pattern assembly; MLI: multi-layer insulation; MRL: main relay lens; PMT: photomultiplier tube; RTU: remote terminal unit; SRL: star mapper relay lens).*

2.3. Payload Hardware

The payload system was divided into eight subsystems (see Figure 2.5). This section provides a brief description of these subsystems, outlining major design features and associated technology.

The payload structure: The payload structure was centred around a box built from five carbon-fibre reinforced plastic (type GY 70), single-skin panels, which provided all necessary interfaces to connect the three mirror mounts, the focal-plane assembly platform, and the various secondary structures. The carbon-fibre reinforced plastic elements gave the payload structure a low thermal susceptibility.

The focal-plane platform was a rigid, carbon-fibre reinforced plastic sandwich plate made of two face sheets of carbon-fibre reinforced plastic bonded on an aluminium honeycomb and equipped with specific inserts used to connect the different focal-plane assembly units—the optical relays, detectors, mechanisms, and electronic boxes. This platform was hard-mounted onto the telescope.

Each of the three telescope mirrors was supported by a mount consisting of a carbon-fibre reinforced plastic frame barrel rigidly connected to the main structure at three points. Three identical flexural-blade systems made of invar and titanium connected the mirror to its barrel.

In addition to the main structure, the secondary structures included the internal baffles, necessary for the protection against straylight, and the heater-mat carriers and covers, which were required to ensure light-tightness of the enclosure and to provide mechanical support to the thermal hardware multi-layer insulation, heater, thermistors and associated harnesses.

The optical units: The telescope optics consisted of the (flat) folding mirror, the spherical mirror, and the beam-combiner mirror, all made of zerodur and light-weighted by about 40 per cent. The optical surface quality of the folding and spherical mirrors was better than $\lambda/60$ rms at a reference wavelength of $\lambda = 550$ nm, and the overall optical quality of the telescope was $\lambda/20$ rms.

The grid assembly was based on a main substrate made of silica. The main grid and the two star mapper patterns were etched into the chromium layer on its front convex face using an electron-beam pattern generating technique. The rear side of the substrate constituted the field lens associated with the relay optics. A set of deviators folded the star mapper beam in the direction of the star mapper relay optics. These elements were mounted on an invar barrel, extended by the focal-plane baffle which protected the elements from stray light.

Relay optics imaged the main grid onto one of the image dissector tube photocathodes. One or other of the two optical chains was selected by means of a Suprasil switching prism, fixed onto a bi-stable positions mechanism, which allowed the beam to be switched between the nominal and redundant channels. Relay optics also conveyed the light from each of the two star mapper grids onto their respective blue/visual photomultipliers. Each of these star mapper relay optics was equipped with a dichroic beam splitter, which provided the colour separation of the beam for the purposes of the Tycho experiment. The selection of the preceding or following star mapper was made electronically.

Also included in the optical units were the internal star pattern assembly which, in conjunction with the switching prism mechanism, gave the possibility of an in-orbit geometric calibration of the deflection coil currents of the main detectors, and the switchable chromaticity filters (one per image dissector tube relay optics), which gave the possibility of an in-orbit measurement of the system chromaticity.

The mechanism units: The re-focusing mechanism held the grid package and an associated folding mirror, which folded the resulting optical beam. This mechanism allowed movement of the grid position with respect to the telescope focal surface. The best focus position, maximising the signal modulation of the two fields of view, was determined in orbit.

The switching mirror mechanism provided the mechanical support to the switching prism, which permitted the selection of either one of the two main detectors.

There were two chromaticity mechanisms, one per image dissector tube channel, each of them being equipped with a chromaticity filter and a broad-band filter of identical optical path length. Switching from the broad-band filter to the chromaticity filter allowed the in-orbit calibration of the instrumental chromaticity.

There were four shutter mechanisms, preventing the detectors from damage induced by light overload as the fields of view scanned the Earth or the Moon.

The detection subsystem: The detection subsystem included the two primary detectors, each of them consisting of an image dissector tube, equipped with its high-voltage power supply and its pre-amplifier combined in a single package, and four photomultipliers, each of them integrated with its own high-voltage power supply and its own pre-amplifier. There were two detection electronic boxes, each of them dedicated to the operation of one main detector assembly and two star mapper detector assemblies (nominal or redundant chains).

The thermal control subsystem: The thermal control subsystem included the multilayer insulation blankets, the heater mats, and the thermistors. All components were installed on the secondary structure. The control law for the heaters was implemented in the satellite on-board computer. Control of heaters and thermistors was performed by the thermal control electronics, part of the service electronics. Twenty-one thermal zones were used to achieve payload thermal control, fifteen being devoted to the telescope enclosure and six to the focal-plane assembly.

The service electronic units: The service electronic units consisted of three boxes located on the upper platform of the spacecraft: (i) the inverter unit, which was used to convert the main DC bus regulated voltage into an AC voltage distributed to the payload electronic boxes (mechanism drive electronics, thermal control electronics, and detection electronic boxes); (ii) the thermal-control electronics, which controlled and monitored the temperature of the payload, using a control law which was implemented in the spacecraft on-board computer; and (iii) the mechanism drive electronics, which controlled and monitored the positions of the payload mechanisms.

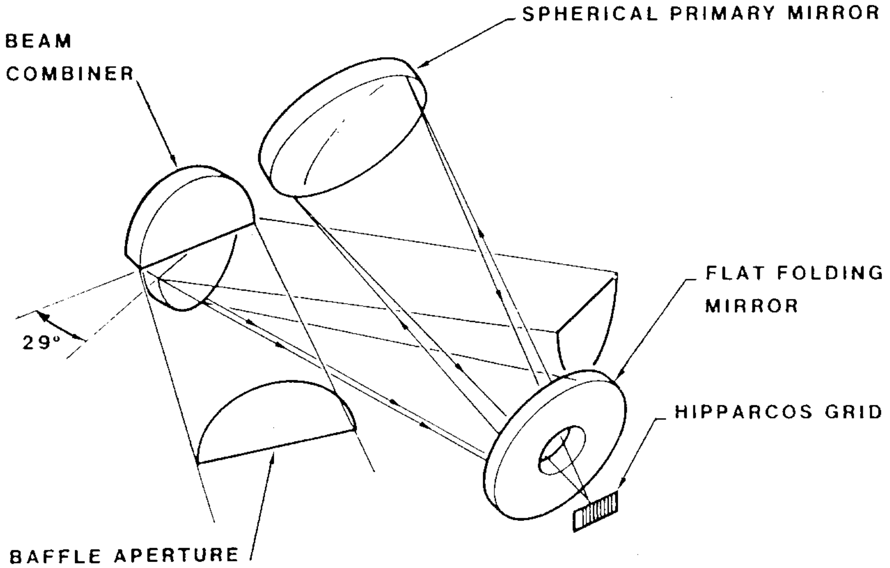

Figure 2.6. *Configuration of the Schmidt telescope. Light entered from the two baffle directions, and was brought together at the beam combiner, which was figured as a Schmidt corrector. The combined light was reflected from the folding and spherical primary mirrors onto the focal surface where the modulating grids were located.*

These three electronic boxes interfaced with the payload remote terminal unit, which was responsible for transfer of data commands and clocks from the spacecraft data-handling system to the electronic units of the payload, as well as the transfer of scientific, engineering and housekeeping data from the payload to the spacecraft data-handling system.

The baffle subsystem: The baffle subsystem consisted of two external baffles, which protected the payload from straylight originating from the Sun, the Earth, or the Moon. They were made of carbon-fibre reinforced plastic and were connected directly onto the spacecraft upper shelf. Each of these baffles was equipped with entrance covers, closed during ground handling and launch. They were opened in orbit by activation of associated pyrotechnic devices.

2.4. Telescope Mirrors

The telescope was based on the all-reflecting Schmidt concept, and consisted of three mirrors: a beam combiner, a primary spherical mirror, and a (flat) folding mirror (Figure 2.6). The folding mirror folded the optical beam to provide a more compact overall configuration. The beam combining mirror also performed the (off-axis) correction of spherical aberration.

A reflective coating was used for all three mirrors. It was chosen for its very high efficiency (in particular in the blue part of the spectrum), together with the fact that it had already been space qualified. It consisted of a layer of Ag, protected by a ThF_4 coating, on a layer of chromium to enhance its adherence. The metallic layer of this coating was grounded by bonding a grounding strap to an area, outside the useful coated

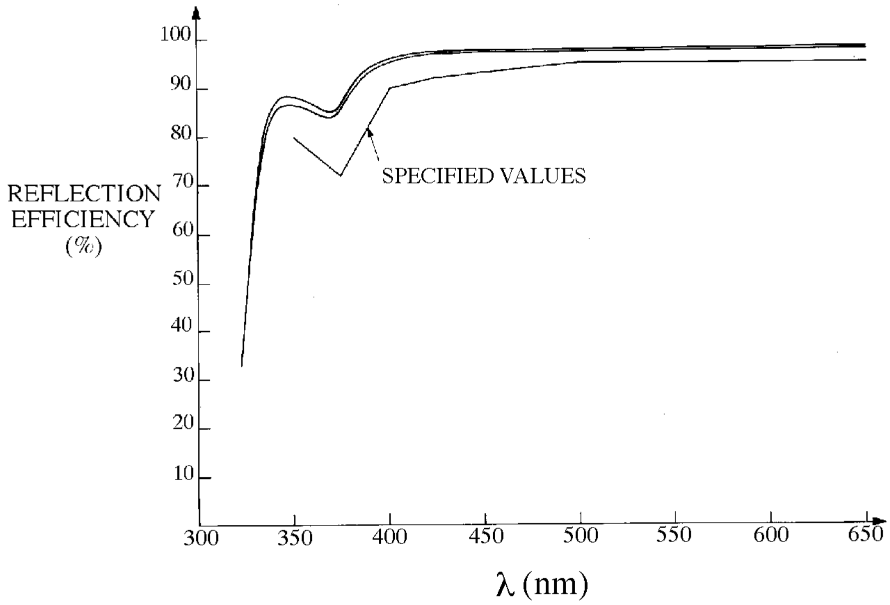

Figure 2.7. *Spectral reflectivity of the mirror coating as a function of wavelength.*

area, which was kept free of the dielectric protective layer. The performances of this coating, in terms of reflective efficiency is given in Figure 2.7. The mirror efficiencies are summarised in Tables 2.2–2.4 as part of the overall payload efficiencies.

The Beam Combiner

The beam combiner had three main functions: to combine the two fields of view; to define the entrance pupil; and to perform the correction of the aberrations of the spherical mirror.

The beam combiner mirror was made from a ‘light-weighted’ polished zerodur blank, 325.6 mm in diameter and 100 mm thick, cut into two halves and reassembled with a wedge angle of 29°. The optical surfaces of the half-mirrors were figured aspherically and the reflective coating defined the pupil area. The beam combiner assembly also included three fixation pads made of invar and bonded to the lateral side of the mirror. These pads interfaced with the beam combiner’s isostatic mounts.

A beam combiner ‘decentre sensor’, consisting of a light source and a quadrant sensor, was bonded onto the two halves of the mirror and was used to align the spherical mirror’s centre of curvature with the aspherical profile centre. The sensor was also used to verify alignment stability during on-ground operations.

The aspherical figuring of the beam combiner was of the Schmidt-Kerber type (see, for example, Buacher 1967). In this design, optical aberrations are minimised by corrections of the optical path at the level of the entrance pupil. The profile (Figure 2.8) was defined by its deviation with respect to the ideal flat surface:

$$X = \alpha\rho^4 + \frac{\beta}{2}\rho^2 \qquad [2.1]$$

where α is the aspherisation parameter ($\alpha = -5.16726 \times 10^{-12}$ mm^{-3}), β is the vertex curvature ($\beta = 3.47724 \times 10^{-7}$ mm^{-1}), and ρ is the radial coordinate in mm.

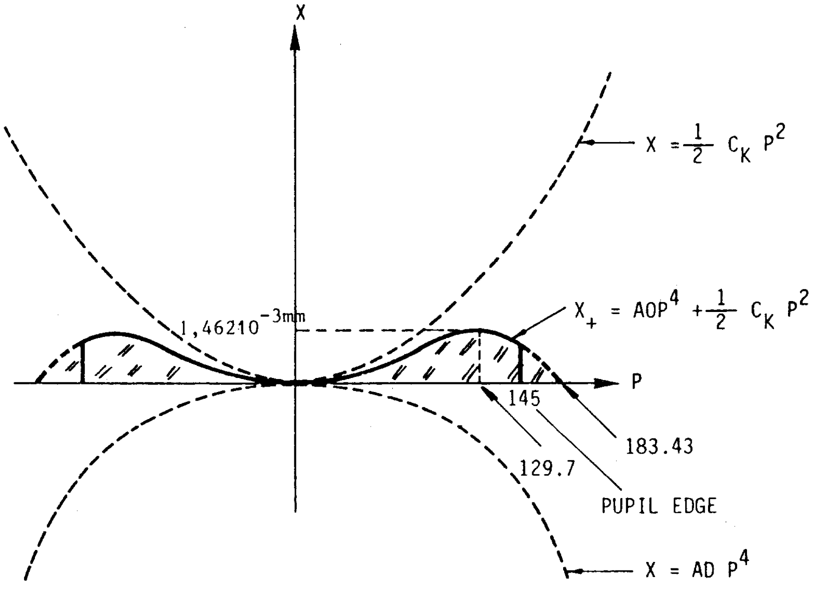

Figure 2.8. *Details of the Schmidt-Kerber profile of the beam combiner.*

Because of the incidence angles of ±14°.5 on the two segments of the beam combiner, the figuring should ideally be elliptical (non-rotationally symmetric) for a perfect correction. This profile was approximated by decentring the rotationally symmetric Schmidt-Kerber profiles of each mirror half by 4 mm from the optical axis, by removing an 8 mm slice while cutting the polished blank. The various steps of the manufacturing process are shown in Figure 2.9.

Deviation of the polished surface, after assembly, with respect to the best-fit Schmidt-Kerber profile (within 1 per cent of the nominal profile), was specified to be less than $\lambda/60$ rms (9.1 nm) at a reference wavelength of $\lambda = 550$ nm. The induced chromaticity was specified to be less than 1 milliarcsec.

Assembly of the two mirror halves was achieved by bonding with 64 glue spots, each 12 mm in diameter and 0.3 mm thick, to minimise wavefront distortions, without affecting the strength of the assembly. After assembly of the two halves of the beam combiner, the pupil projection onto a plane perpendicular to the optical axis, gave an external contour diameter of 290 ± 0.5 mm. Thus, the reflective coating external contour on the half mirror optical faces was actually elliptical.

The Flat Folding Mirror

The folding mirror was made from a flat, 'light-weighted' zerodur blank, 356 mm in diameter, 60 mm thick, with a conical central hole. Three fixation pads, made of invar, were bonded to the lateral side of the mirror. The mirror was polished by an annular lap technique, with appropriate compensation made for the weight of the fixation pads. Deviations of the resulting polished surface with respect to the best-fitting residual sphere (which had a radius of curvature greater than 100 km) were less than $\lambda/60$ rms. Induced chromaticity was less than 1 milliarcsec. The folding mirror was mounted to a plate, which had a large oval cutout for weight reduction. Two brackets were provided to hold the mirror in the mounting plate, and adjustment was possible from outside the barrel at three points.

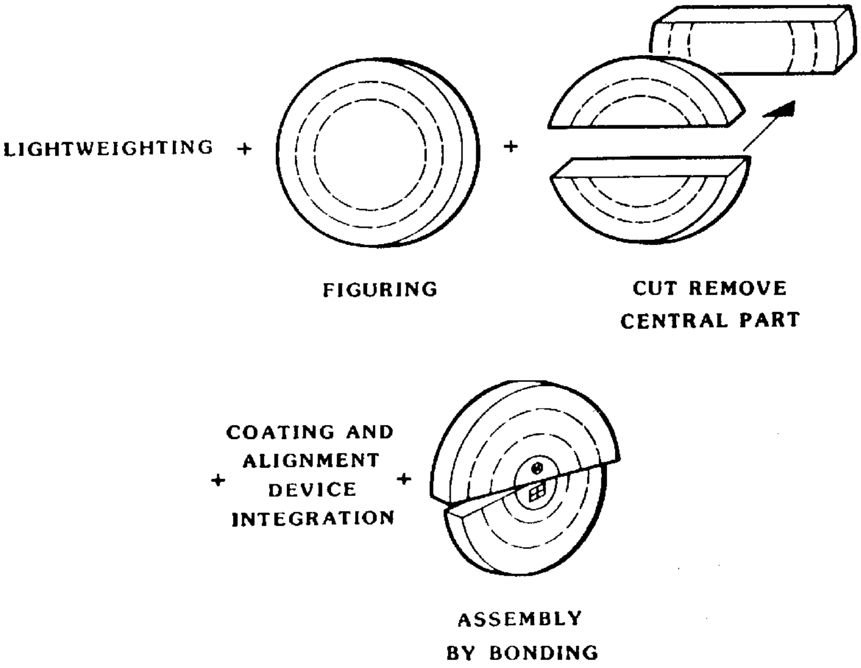

Figure 2.9. *Steps in the manufacture of the beam combiner. All three steps provided a considerable technical challenge in order to retain the overall high quality of the optical wavefront.*

The Spherical Mirror

The spherical mirror was made from a 'light-weighted' zerodur blank, 393 mm in diameter, 66 mm thick, with a small central hole (for alignment purposes). The optical surface was of concave spherical shape. Three fixation pads, made of invar, were bonded to the lateral side of the mirror. A lens, called the beam converger, was bonded to the central part of the rear side of the mirror, and this allowed for stability testing of the telescope, between the spherical mirror and the grid assembly.

The mirror was polished by conventional techniques, with appropriate compensation made for the weight of the fixation pads. Deviations of the resulting polished surface with respect to the best-fitting sphere (with radius of curvature 2800 ± 3 mm) were less than $\lambda/60$ rms. Induced chromaticity was less than 1 milliarcsec.

Beam Combiner and Mirrors Fixation Pads

The invar fixation pads of the mirrors and of the beam combiner were designed to minimise the wavefront distortion induced during the integration of the mirrors in their barrels with the isostatic mounts. They were bonded to the sides of the mirror with a glue film (type EC 2216) 0.3 mm thick. This resulted in a lack of symmetry in the (three-point) mounting of the two halves of the beam combiner.

The fixation pads were 50×70 mm^2 in size, with a thickness of 14.2 mm. They were tightened to isostatic mounts by twelve M4 studs, and positive locking was achieved by means of two expandable pins per pad. To avoid induced wavefront distortions, the interface plane flatness was specified to be better than 2 μm, the studs were not fully secured to the pads, and expandable pins were located outside the main body of the pads. Overall wavefront error maps were measured as part of the verification procedures.

2.5. Modulating Grid and Baffle Unit

The grid assembly (Figure 2.10) was composed of the baffle unit and the grid unit. The main function of this assembly was to provide a modulated star signal which was analysed by the detection electronics (main detector assembly, star mapper detector assembly and detection electronic boxes). Consequently, the global performances of the payload were directly linked to the performance of this assembly. During the mission lifetime, the position of the grid unit with respect to the telescope focal surface could be adjusted by means of the refocusing mechanism, to compensate for secular shrinkage of the telescope structure due to outgassing, and other effects (see Chapter 10).

The Baffle Unit

The primary function of the baffle unit was to provide straylight protection of the modulating grid. A secondary function was to protect the grid against dust raised during integration and a specific ‘dust cover’ was implemented. This dust cover could be opened and closed manually from outside the payload, and was opened just before launch by disconnecting the actuating wire. The cover was equipped with a redundant spring system to keep it open during launch and thereafter throughout the mission. The baffle unit was also equipped with ‘grid reference marks’ and corresponding light sources, and a set of ‘auto-collimation slits’ and corresponding light sources.

The focal-plane baffle supported the light sources and optics used to illuminate the grid reference marks and auto-collimation slits, and also provided a base for the dust-cover mechanism. The complete baffle unit, with the exception of the dust cover, was made of invar.

The baffle structure itself was a tube, partly cylindrical and partly conical, from which a large part of the conical section had been removed. At the cylindrical part were lugs which formed the interface to the grid unit and the grid support of the refocus mechanism.

Inside the cylindrical part of the baffle, three diaphragms were positioned at distances of 6.5, 20, and 35 mm from the grid to provide straylight protection. The two baffle plates nearest to the grid surface were equipped with holes to fix the tubes in which the light-emitting diodes of the grid reference marks and auto-collimation sources were mounted.

The dust cover was mounted on the baffle tube with three screws and was operated manually via a double wire actuator system. It was designed to withstand vibration loads in both its closed and open positions. The pre-loading of the two springs was such that cover movement due to vibration was negligible. The dust cover was also approximately balanced about its hinge by the use of two counter-weights made of tungsten, fixed at the ends of two lever arms. In its closed position, the ‘labyrinth’

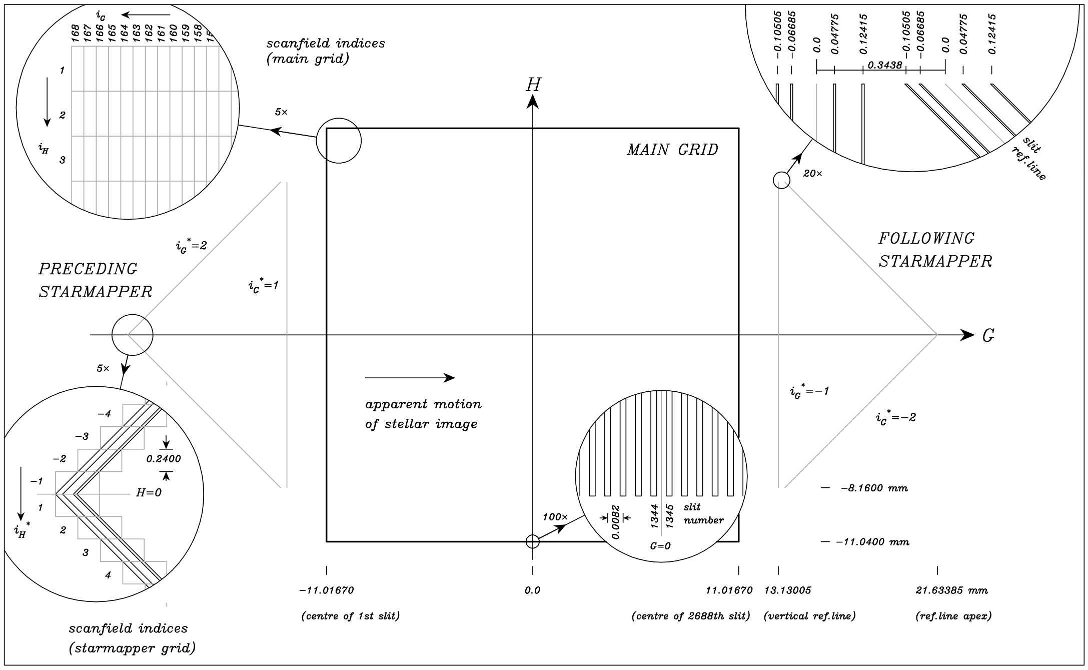

Figure 2.10. *General layout of the main and star mapper grids. The main grid covers a field of* $0\overset{\circ}{.}9 \times 0\overset{\circ}{.}9$ *(central square region) comprised of 2688 transparent and opaque slits (see central detail), layed down as* 46×168 *distinct 'scan fields' (see detail at top left). The two star mapper slit systems (two being provided for redundancy) each comprise 4 vertical and 4 inclined aperiodically spaced slits.*

formed between the edge of the cover and the edge of the third baffle plate prevented dust from entering the grid box.

The Auto-Collimation Sources

An auto-collimation device was provided within the payload to simulate a star image at the grid level. It was operated only while the satellite was on the ground. The sources were attached to the first baffle plate and illuminated by a light-emitting diode mounted in a tube between the first and second baffle plates. Each auto-collimation source consisted of a rectangular slit, $5\times200\ \mu\mathrm{m}^2$ in size, and two prisms; one providing illumination of the slit and one projecting the auto-collimation source beam outward, in the direction of the optical axis. The dimensions were such that the auto-collimation source-slit appeared to be located on the grid surface. The photon flux, measured at the sub-assembly level, was more than 3×10^7 photon s^{-1}.

The auto-collimation source was made using an electron-beam pattern generator on a standard chromium-coated glass plate of the type used for integrated-circuit masks. After writing and etching, the plate was cut, ground to the required size, and bonded between the two prisms. This sub-assembly was then bonded to the first baffle plate, using a bonding jig to ensure accurate positioning. As the area available for bonding was only an annulus of 18 mm diameter, a titanium bracket was placed over the prisms to keep them properly located, even in case of a failure of the bond. A secondary purpose of this bracket was that of straylight protection.

The associated series of resistors and interconnections was located on a printed-circuit board that was attached to the linear actuator. The wiring between this printed-circuit board and the baffle unit was routed via a 15-pin connector, so that the baffle unit could be detached from the refocus assembly. The connector was located in the plane of the focal-plane assembly-platform in such a way that removal of the baffle unit was possible when the refocus assembly was mounted on the focal-plane assembly platform. The replacement of light-emitting diodes, bonded to the baffle, was possible during ground operations.

The Grid Unit

The grid unit was the main optical part of the refocusing assembly. It consisted of the optical block on which the main modulation grid and the star mapper patterns were written; the two star mapper deflectors; and the mounts for the optical block and for the star mapper deflectors. The grid transmissions for the main and star mapper detection chains are shown as part of the overall payload detection efficiencies in Tables 2.2–4.

The optical block was a piece of Suprasil 1, a high-quality silica. It served both as a substrate for the grid and the star mapper slits, and also as a field lens—i.e. the first element of the optics between the grid and the image dissector tube. The grid and the star mapper slits were written on a convex surface, matching the curved focal surface of the telescope. As this surface constituted a carrier for a pattern with sub-micron accuracy, which, to a large extent, defined the achievable accuracy of the mission, an extremely smooth surface finish was required. The optical block polishing was followed by a ‘superpolish’ treatment of the critical grid area defining the main field pattern. After polishing and cleaning, a layer of chromium was sputtered on the surface, followed by the deposition of a layer of electron-sensitive resist.

The rear side of the optical block had three parts. The central area, opposite the grid, was polished to a radius of curvature of 213.8 mm and served as a field lens. The parts opposite the star mapper patterns were flat and recessed to provide room for the star mapper deviators.

The optical block was bonded in the grid mount with the aid of a bonding rig that allowed accurate positioning of the optical block and the grid. An electrical contact between the chrome of the grid pattern and the grid mount was also provided.

A set of grid reference marks was provided within the grid assembly, allowing partial geometrical calibration of the detector assembly in flight. The grid reference marks were two holes, $275 \times 275\ \mu\text{m}^2$ in size, located on the grid surface. Each of them could be illuminated by one of two light-emitting diodes (for redundancy reasons) via an opal glass diffusor mounted on the first baffle plate.

The light-emitting diodes were mounted inside invar tubes, a mechanically rigid mounting that also prevented straylight from the light-emitting diode reaching the grid. The photon flux from these diodes, measured at the sub-assembly level, was more than 5×10^7 photon s^{-1}.

The grid pattern consisted of the main grid and star mapper grid patterns. The main characteristics of the parallel slits of the main grid are given in Table 2.5. Although the required grid pattern was uniform over the main field of view, it was written in discrete ‘scan fields’, 46×168 of these scan fields covering the full field of view (the dimensions

Table 2.5. Summary of the calibration results of the main grid.

Item	Performance
Slit geometry:	
average grid period	8.20 ± 0.001 μm
average slit width	3.13 ± 0.03 μm
slit width standard deviation	< 0.033 μm (rms)
total number of slits	2688
number of scan fields	46×168
scan field dimensions	131.2×480 μm^2
Medium-scale grid irregularities:	
M_{pq}	$-0.038 < M_{pq} < 0.053$ μm
gradient (scan field to scan field)	0.009 μm (rms)
Small-scale grid irregularities:	
individual slit (random)	0.015 μm (rms)
regular ‘saw tooth step’	0.000 μm (mean value)
irregular ‘saw tooth step’	0.016 μm (rms)
correlated scan field orientation	0.009 μm (rms)
uncorrelated scan field orientation	-0.009 μm (mean value)
Grid reference marks:	
shape	square
edge dimension	22.04–22.08 mm
centering accuracy	±0.001 mm
orientation	±0.25 arcmin

Table 2.6. Summary of the principal specifications for the star mapper grid.

Item	Specification
Medium-scale grid irregularities:	
vertical	< 0.5 μm (max)
inclined	< 0.5 μm (max)
transverse gradient (vertical)	< 0.077 μm (rms)
transverse gradient (inclined)	< 0.077 μm (rms)
Small-scale grid irregularities:	
vertical	< 0.05 μm (rms)
inclined	< 0.05 μm (rms)
magnification factor	< 0.15 (max)
scan field orientation (vertical)	< 0.034 μm
scan field orientation (inclined)	< 0.034 μm
slit width value	6.20 μm
slit width variation	< 0.35 μm (max)
Grid calibration:	
vertical	< 0.055 μm (rms)
inclined	< 0.077 μm (rms)

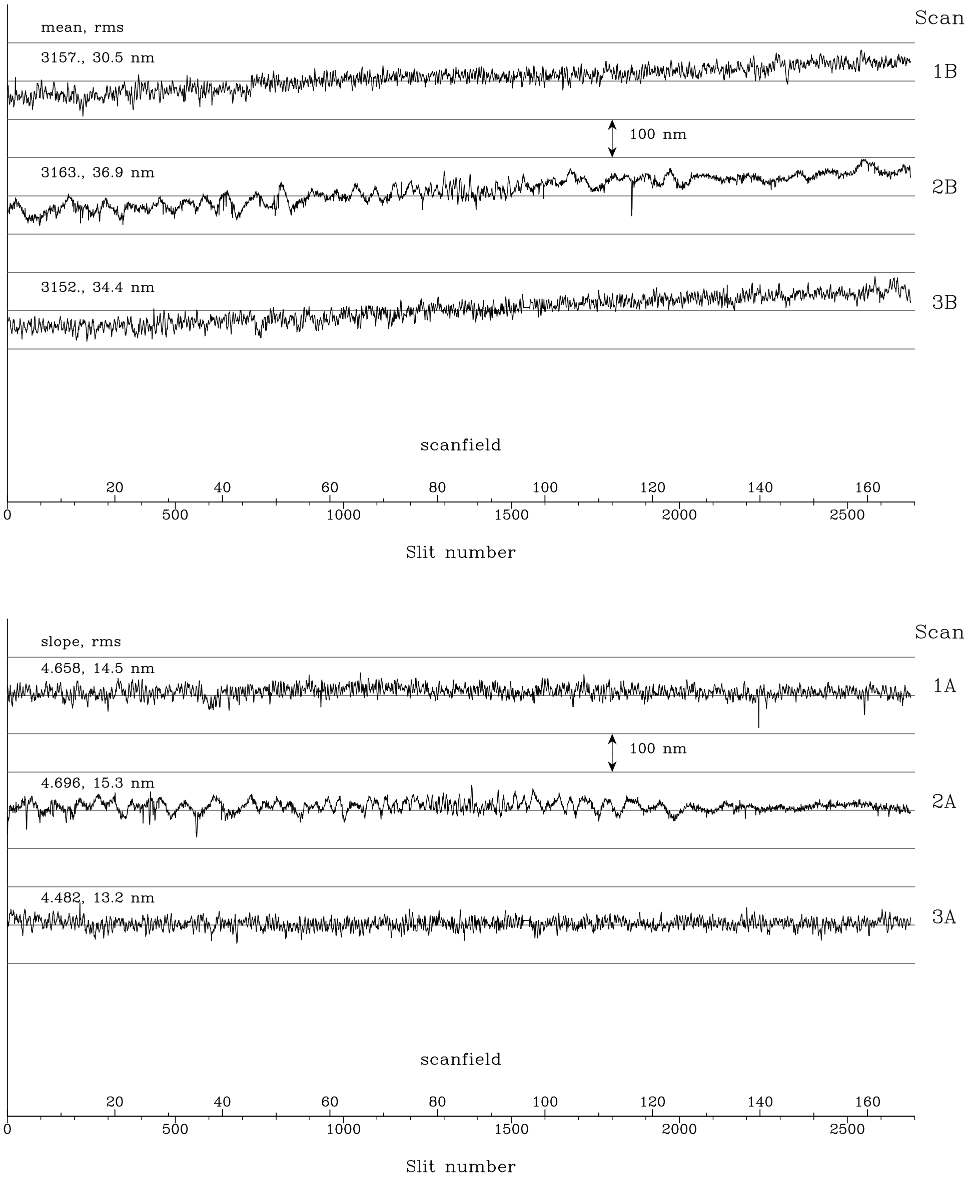

Figure 2.11. *Slit width variation across the main field. Top: as measured; bottom: after removal of the linear component. Nine calibration scans were made (on ground), three each (A, B, C) at $i_H = 1$ (1), $i_H = 23$ (2) and $i_H = 46$ (3) (see also Figure 2.10). The abscissa is given in both scan field and slit numbers, and the scale of the ordinate is shown in the figures. In the top figure the mean slit-width and associated rms values (in nm) are also given. In the bottom figure the (corrected) slope (in nm(width)/mm), and the rms values of the slit-width after removal of the slope, are given. The figure illustrates the high quality of the modulating grid, and the remaining medium-scale structure in the grid (due to the scan field construction) which was accounted for in the medium-scale calibration on ground and in orbit.*

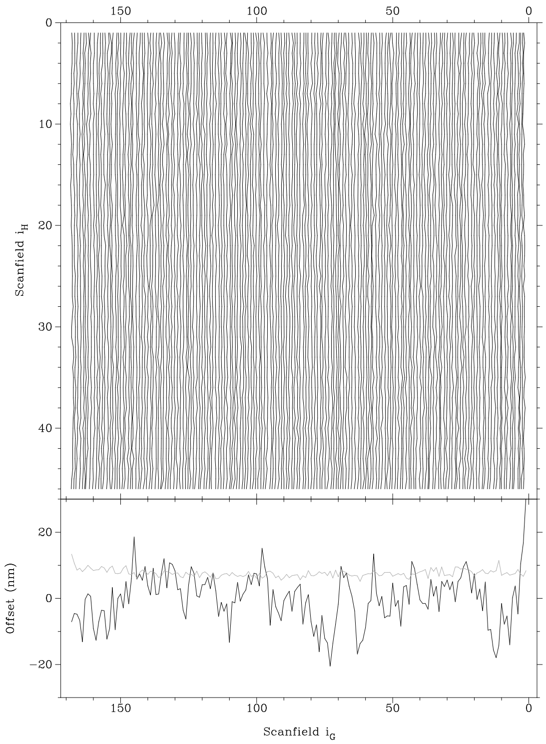

Figure 2.12. *The medium-scale irregularity of the main grid, in the scan direction. The geometry of the grid corresponds to the configuration shown in Figure 2.10. The scale in the upper figure is such that one scan-field 'unit' corresponds to 40 nm. The lower figure shows the mean value in the scan direction (solid line), and the standard deviation (dotted line).*

of each scan field were $131.2 \times 480\ \mu\mathrm{m}^2$, with the longer dimension in the direction of the slits, i.e. normal to the scan direction). Two star mapper patterns lay on either side of the main grid—their principal characteristics are summarised in Figure 2.10.

Considerable attention was given to the manufacture and calibration of the grids, given that the final mission accuracies of around 1 milliarcsec corresponded to approximately $0.007\ \mu$m at the focal plane. Deviations of the main grid from a perfectly regular one were classified into large, medium, and small-scale grid irregularities. The large-scale grid irregularities were defined as deviations that could be expressed as a second-order polynomial fitted to the distortion map—these could be calibrated by the data reduction consortia during the 'great-circle' step of the data reductions. The medium-scale grid irregularities were defined as a matrix of M_{pq} elements, where each element represented the average distortion of the scan field (p, q) after removal of the large-scale component. The range of M_{pq}, and its field-to-field gradient, are tabulated in Table 2.5.

Small-scale grid irregularities were defined as the residual distortion, after the removal of the large- and medium-scale components. Their characterisation would have required a very large ground calibration effort, followed by the correction of the satellite data at a very high spatial resolution. The grid manufacture concentrated on producing a grid in which the small-scale irregularities could be neglected, a fact eventually confirmed in orbit. In the manufacturing and calibration process, the small-scale irregularities were split into various components (see Table 2.5). The 'individual slit' contribution

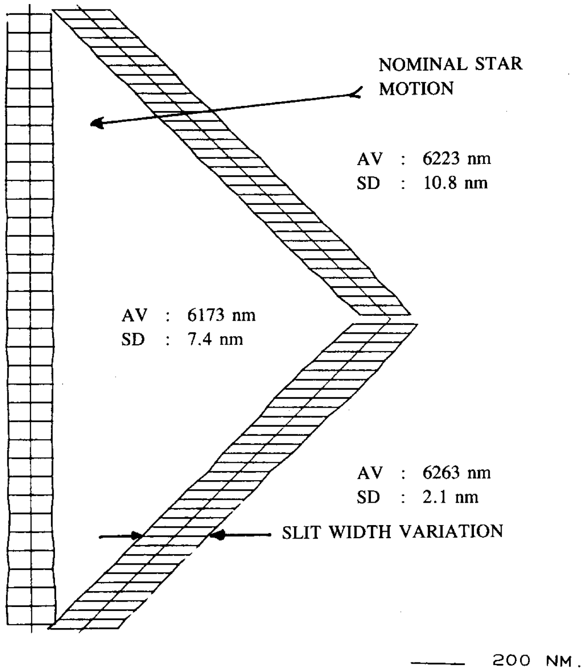

Figure 2.13. *Representation of the slit width variation for one vertical and one chevron slit of the preceding star mapper.*

arose from the imperfections in the slit edges. The regular and irregular 'saw tooth step' contribution was a result of the scan field 'scale' not being precisely matched to the scan field centre-to-centre spacing. The correlated and uncorrelated scan field orientations, measured in microns at the corners of the scan fields, arose from misalignments in the individual scan field orientations.

The grid pattern was written by means of an electron-beam pattern generator machine. A computer program for the writing of patterns with sub-micron accuracy on a curved surface was developed specifically for this purpose. According to the grid manufacturing plan, a first pilot series was produced in order to optimise the manufacturing process, followed by a second pilot series to finalise the process. This second pilot series was intended to lead to a grid of flight standard. A third pilot series was eventually produced, due to problems encountered during second-batch operations. Following the pilot series, a series of five flight-standard grids was made, from which the flight and the flight-spare grids were selected.

After writing, the grid was subjected to an extensive calibration process, in order to verify the quality of the writing. The measurements were made by optical and electron-beam methods. The main grid calibration results related to the slit width value, which was measured in three ways: using optical diffraction equipment, electron-beam pattern generator, and microscope. An optical inspection was also carried out to verify the pattern quality and to assess the distribution of any pattern defects, the pattern position and orientation, and the optical transmittance.

The electron-beam measurements used a dedicated software package. The principal element in this software package was the marker search by the electron-beam pattern

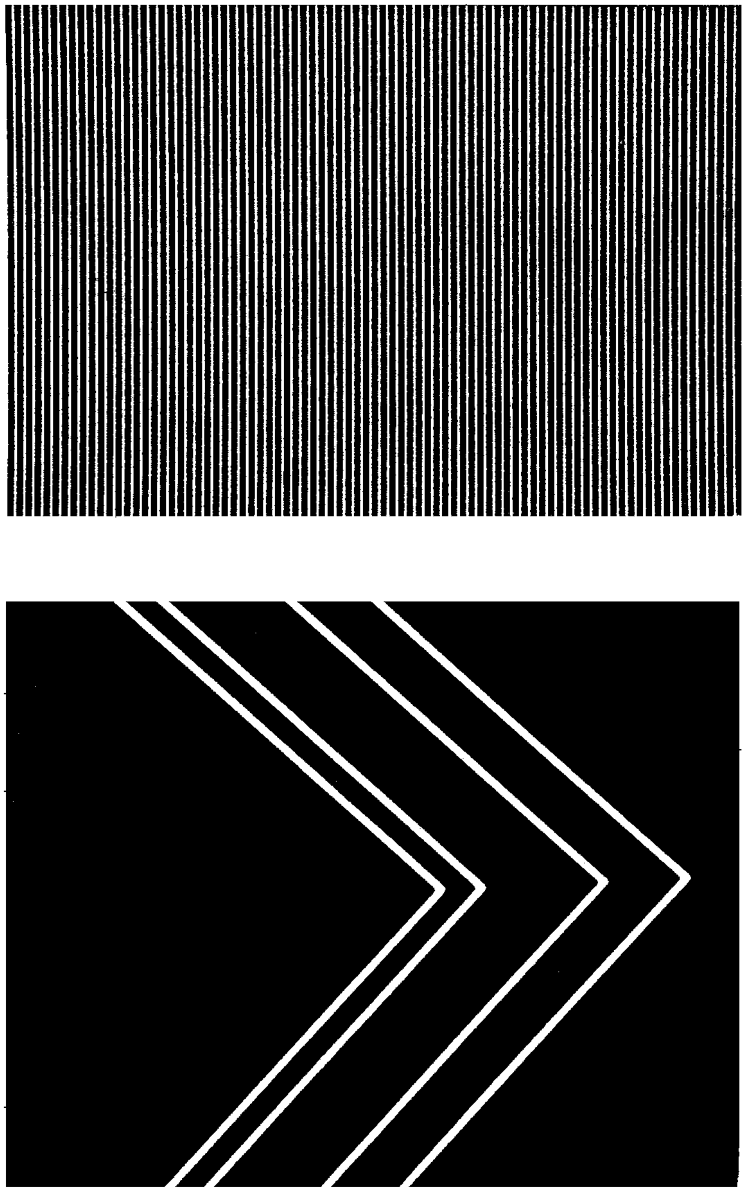

Figure 2.14. *Optical micrographs of part of the main modulating grid (top figure) and the star mapper grid (lower figure). The grids represented one of the main technical challenges of the Hipparcos payload, and were of an extremely high quality.*

generator. Another important element was the 'almost undeflected electron-beam operation', in order to minimise the contribution of main beam deflection errors. As a consequence, an *xy* table movement was required for each slit or marker measurement. The location of the position-calibration markers was obtained with an accuracy of 10 nm rms from its four marker edge positions. Each edge position was the average of 20 measurements on a centred 10 μm part of the marker edge. The marker search algorithm was based on a signal bandwidth reduction and a binary search scheme.

The slit position was obtained with an accuracy of 10 nm rms by the same marker search algorithm applied to both slit edges. The parameters were adapted to fit the nominal slit sizes. In the main grid pattern, each slit edge position was derived from an average of 21 measurements over an edge distance of 6 μm, corresponding to the size of an imaged star in the direction of the slits. The position of each slit was obtained as the mid position of the slit edge positions, and the width of each slit was the difference of the corresponding slit edge positions.

The expected slit position was obtained for the known pattern positions in the grid coordinate system. The beamwriter coordinate system was transformed to the grid coordinate system by the compensation sequence of the beamwriter. The reference zero-point was the location of the position-calibration marker. The main grid and star mapper patterns for the electron-beam measurements have the same scan field xy arrangement as the one used during the pattern writing. Within a scan field, the slit position was defined by the x-position and the slit number.

The value of the measured slit position minus the expected slit position was obtained for the selected slit within the scan field. The positions measured within the main grid pattern relate to the matrix of 46×168 scan fields. For all scan fields, one slit at the scan field centre was measured. By repeated measurements with 8 slits per scan field, it was demonstrated that the same value of the scan field parameters had been achieved. It was demonstrated that just one measurement near the scan field centre was adequate to measure the scan field centre position. The idea behind this electron-beam measurement process was the 'step-on and repeat' process of the same scan field during writing, without a change in the scan field parameter settings. This procedure also helped to keep the electron-beam measurement time within reasonable limits, without a loss in accuracy of the position results obtained.

The grid calibration results are summarised in Table 2.5 for the main grid pattern, and the specifications related to the star mapper grid are summarised in Table 2.6. The electron-beam measurement data were recorded on magnetic tape for subsequent calibration studies, and distributed to the data reduction consortia, who used the geometrical calibration parameters during the ground processing of the satellite data. Examples of the grid calibration data for the main field are given in Figure 2.11 (the measured slit width variation across the grid), Figure 2.12 (the measured variation in the medium-scale irregularity across the grid), and Figure 2.13 (the measured slit width variations for the star mapper). Optical micrographs of part of the actual flight grid are shown in Figure 2.14.

The Star Mapper Deflectors

The light from the star mapper slits was deflected sideways, on to photomultipliers at either side of the refocus assembly, by star mapper deflectors mounted directly behind the optical block. Each star mapper deflector had a convex side, facing the optical block, which acted as a field lens. The other side, which was flat, deflected the light by 90°.

The star mapper deflectors were made from BAK 1 glass, which has a large refractive index, ensuring total internal reflection. The thermal expansion of 7.6×10^{-6} K^{-1} was accommodated by the deflector mount and the use of an appropriate flexible adhesive (Araldit AV138M). The bonding was carried out in a bonding jig to ensure proper alignment. The star mapper deflectors were appropriately masked to prevent straylight. In order to limit the Cerenkov effect, a further mask was directly replicated on the star mapper deflectors.

The Grid and Deflector Mounts

The grid mount was the housing for the optical block and formed the interface between the optical block, the baffle unit, links for parallel movement, and the star mapper deflector holders. The grid mount was a holder made of invar, suitable for carrying the optical block, without distortion and with the least possible introduction of displacements or stresses as a result of the thermal behaviour. This was achieved by using 24 bonding areas at the circumference of the lens. Mounting and dismounting of the grid unit and the baffle unit was possible while the refocus assembly remained attached to the focal-plane assembly platform.

In order to eliminate electrostatic charge build-up on the grid surface, four grounding wires were bonded to the grid (using Ecobond 55C), the other ends being bonded to the grid mount. The star mapper deflectors were mounted in their holders with Araldit AV138M glue with hardener HV 998. They were positioned with the help of an assembly-rig, and then bonded to the holder.

2.6. Relay Lens Systems

Various relay lenses and optical components were used to transfer the light modulated by the grid onto the detectors: the image dissector tube relay lenses, the photomultiplier relay lenses, the internal star pattern assembly (which was used for calibration purposes), and the associated filters and dichroics. A schematic layout of these various optical components is shown in Figure 2.15, which also shows the configuration of the B_T and V_T star mapper channels.

Image Dissector Tube Relay Lens

Optical design: The layout of the image dissector tube relay lens is shown in Figure 2.16. The energy contained in a circle of given diameter was computed from the geometrical size of the image blur. The spectral weighting factors used to represent a star of colour index $B-V = 0.5$ mag are given in Table 2.7. The results obtained are given in Table 2.8. The transmission budget for the image dissector tube relay lens is given as part of the overall payload transmission summarised in Table 2.2.

Multiple reflections within the relay lens system, and between the relay lens system and the other optical components, could induce ‘ghost images’, more or less focused, within the field. These were studied, and the relay lens design optimised to reduce the most severe ghost images (such as that arising between the lens system and the photocathode) to acceptable levels, by adding appropriate anti-reflection coatings to the lenses. The design also took into account an ‘oversizing’ to account for collection of the maximum amount of light, including that diffracted by the grid.

Each of the two image dissector tube relay lenses imaged the focal surface of the telescope onto the photocathode of the image dissector tube. The main housing of each lens assembly was machined from aluminium and supported the single lens mounts. A locking ring kept each set of lenses in a well-defined position. The outer faces were milled to a polygonal form. All attachment threads for fixation assemblies were reinforced with

Helicoil MN3. Shielding required for the protection of the glass against high-energy electrons creating Cerenkov radiation was also fixed to the housing with screws.

Between the two blocks of lenses, a deep cutout provided space for an aperture stop and filters. Each individual lens of the optical relays was mounted separately in a mounting ring to which the lens was bonded with Zeiss ADM5A glue. All mounting, securing, and locking rings had venting holes to allow depressurisation after launch. Each mounting ring had one radial fitting face and two plane parallel axial fitting faces. These machined faces were used for centering and tilt adjustment after bonding of the lens.

The image dissector tube relay lenses were fixed onto the focal-plane assembly platform by means of three similar feet, each with a titanium spring blade providing flexibility. Adjustment was permitted by built-in eccentric washers at the bases of these three blades, which could be positively locked after adjustment.

The image dissector tube switching prism was used in two different modes: in the nominal mode, the grid was imaged onto the photocathode of the main detector after reflection on its reflective front face, while in the internal star pattern assembly mode, the rear side of the reflective surface was used to image the internal star pattern onto the image dissector tube. Depending on the position of the prism, one detector viewed the grid, while the other viewed the internal star pattern, or vice versa.

The switching prism material was Suprasil 1 silica. The mirror support ‘barrel’ was made of invar. The sides of the prism were coated with an anti-reflective coating with a reflection loss of less than 0.5 per cent. On the outer side of the prism, an aluminium layer was deposited on the Suprasil, resulting in a reflection efficiency of better than 90 per cent, at wavelengths longer than 400 nm. This was followed by the deposition of the outer reflective layer, comprising a silver coating and a dielectric layer, which provided the reflection surface for the nominal path. The internal star pattern beam passed through the prism and was reflected by the aluminium layer.

The switching prism was bonded onto its invar mount with Zeiss Kleber No. 51 glue cured at room temperature. The cure time was 24 hours, and a film thickness of 0.1 mm was used. The bonded and mounted prism was balanced by a counterweight, adjusted by means of three screws permitting fine tuning of the prism’s centre of gravity.

Photomultiplier Relay Lens

Each of the two photomultiplier relay lenses imaged the entrance pupil of the telescope onto the photocathode of two photomultipliers. The lenses, mirrors, filters, and the baffle were mounted in a U-shaped barrel with two exit lenses. Space for dichroic filters was provided in the barrel. The transmission budget of the photomultiplier relay lenses, for the B_T and V_T channels, is shown as part of the overall payload transmission in Table 2.3 and Table 2.4, respectively.

The main housing consisted of a U-shaped support machined in stainless steel. The necessary shielding to provide the protection against Cerenkov radiation was clamped to it. All optical parts were mounted separately on this main housing. After removal of the top cover, all optical elements were easily accessible for adjustment. All attachment points for fixation assemblies, optical parts, and the shielding were reinforced by increased wall thicknesses. The main housing also provided the necessary interface points for the fixation of the dichroic elements. All optical parts could be separately adjusted.

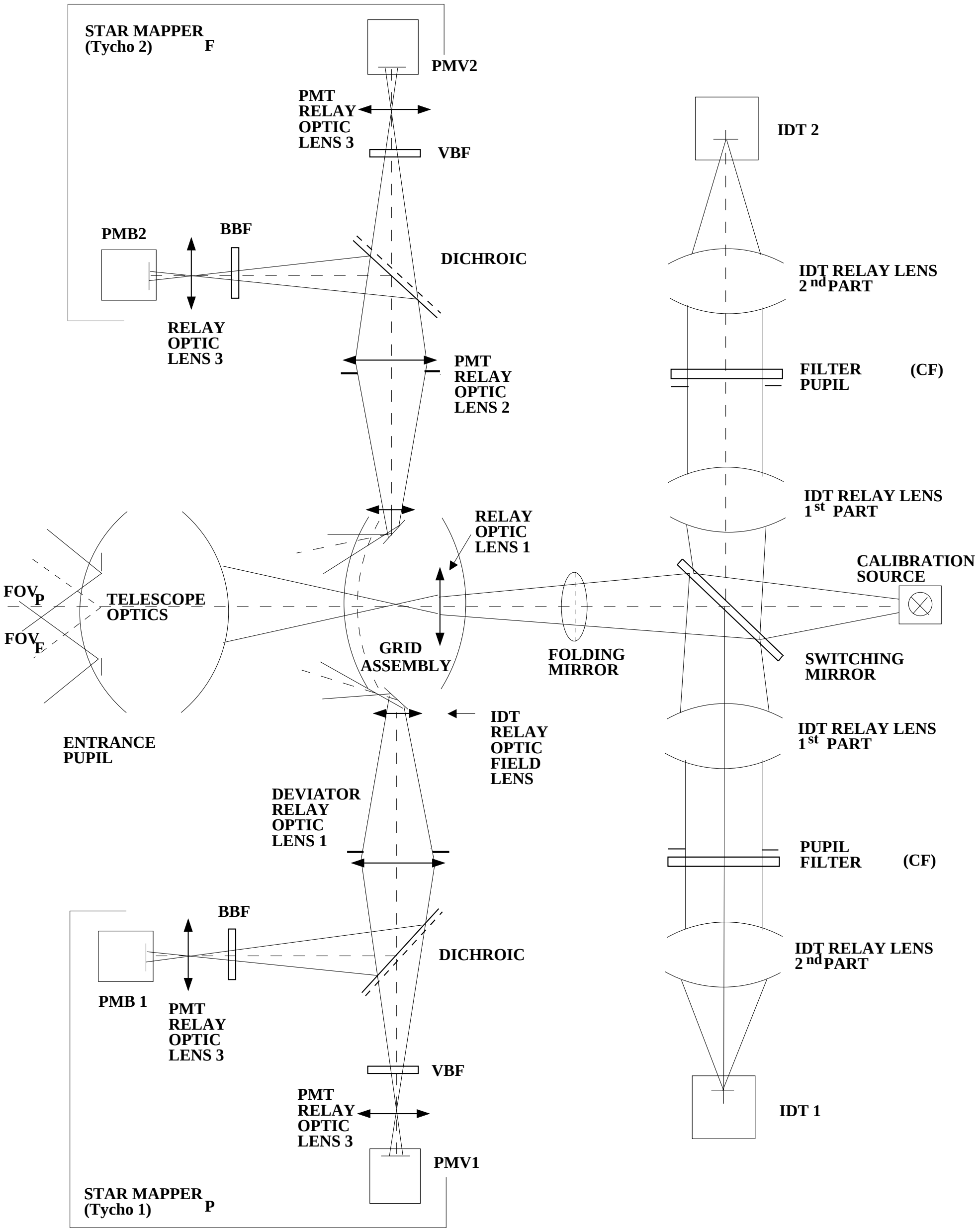

Figure 2.15. *Schematic of the optical units in the focal-plane assembly.*

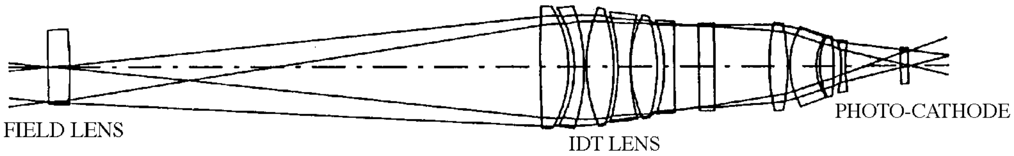

Figure 2.16. *Layout of the image dissector tube relay lens.*

The interface with the focal-plane assembly platform consisted of two spring blades for flexibility, and a third fixed point. Adjustment was achieved by eccentric washers at the base of the blades and fixed point, which were positively locked.

One lens had its own adjustment capability (shift of 2 mm in the X and Z directions and tilt of 5° about the X and Z axes). The bracket rested with its spherical face (the centre of sphere was the centre of the lens) in a spherical cap. Tilting and fixation of the lens was effected with four screws on the rear face of the mount. Lateral and vertical adjustment was made relative to a frame fixed to the barrel. Adjustment was positively fixed with tuned plates.

Internal Star Pattern Assembly

An internal 'fiducial' star pattern assembly was incorporated into the payload to allow in-flight calibration of the transformation from grid coordinates to deflection coil currents of the main detector assembly.

The internal star pattern was projected onto the photocathode of the main detector assembly to be calibrated. This assembly then scanned the fiducial star pattern, while the output data and the corresponding deflection currents were transmitted to ground. From these data, the relation between the deflection currents and the optical coordinates, as defined by the internal star pattern assembly, was derived. What were really needed however, were not the internal star pattern assembly coordinates, but the grid coordinates. For that reason, the optical path between the star pattern in the internal star pattern assembly and the main detector assembly was an exact duplicate of that between the grid and main detector assembly.

The switching between calibration and observation of the grid was done by the same switching mirror that deflected the grid output to either of the two redundant main detector assemblies. The thickness of the mirror was essentially zero, but the presence of the glass prism, supporting the mirror surface in the optical path between internal star pattern assembly and main detector assembly, made it necessary to apply a correction to the path length.

The internal star pattern assembly consisted of two major parts: a star source, containing the star pattern, a light diffusor, and two sets of light-emitting diodes; and a frame, supporting the star source and two folding mirrors. This frame also carried the electrical connectors. It had three adjustable feet, constituting the interface with the focal-plane assembly platform and providing an alignment facility.

During calibration, the star pattern was substituted for the main grid in such a way that the optical path from the star pattern to the main detector assembly optics was nominally equal to that from the grid. The only difference was that a correction was applied due to the fact that the glass prism, supporting the switching mirror, was in the internal star pattern assembly optical path and not in the grid one. The very limited space available made it necessary to fold the optical path twice, a function performed by two flat mirrors in the internal star pattern assembly. Also, the substrate carrying the star pattern had the same dimensions as that carrying the grid and was made from the same material.

The star pattern consisted of 275 μm square holes on a regular square grid with a 2.2727 mm pitch, resulting in a projected pattern of light spots with 1 mm pitch on

Table 2.7. Weighting factors for the different wavelengths used, defining the input flux corresponding to a star of colour index $B - V = 0.5$.

Wavelength (nm)	375	450	550	650	750
Weights	0.23	0.97	0.88	0.55	0.18

Table 2.8. Image dissector tube relay lenses encircled energy in the image plane (the image point is defined as the centre of 'gravity' of all points in the spot). In all cases, the energy within 80 μm diameter is close to 100 per cent.

Object Point		Image Point		Energy within
X (mm)	Y (mm)	X' (mm)	Y' (mm)	40 μm diameter (per cent)
0.0	0.0	0.000	−0.001	99
6.0	6.0	−2.616	−2.615	99
6.0	0.0	−2.613	0.000	98
6.0	−6.0	−2.612	2.614	98
0.0	0.0	0.000	−2.615	100
0.0	−6.0	0.000	2.611	97
8.0	8.0	−3.492	−3.488	99
8.0	0.0	−3.485	0.001	98
8.0	−8.0	−3.485	3.488	98
0.0	0.0	0.000	−3.488	100
0.0	−8.0	0.000	3.483	97
11.0	11.0	−4.810	−4.803	96
11.0	0.0	−4.796	0.003	98
11.0	−11.0	−4.797	4.804	97
0.0	11.0	0.000	−4.800	100
0.0	−11.0	0.000	4.792	97
12.0	12.0	−5.242	−5.242	94
12.0	0.0	−5.232	0.004	98
12.0	−12.0	−5.235	5.244	96
0.0	12.0	0.000	−5.238	100
0.0	−12.0	0.000	5.229	97

the main detector assembly cathode. The pattern was defined by an electron beam pattern generator and etched in a chronium layer, vacuum deposited onto a bi-convex lens made of Suprasil 1 (fused silica). The material and the dimensions of this lens were the same as those of the grid substrate. The manufacturing of the star patterns was done in parallel with the manufacture of the main and star mapper grids.

The star pattern was mounted inside an invar tube and illuminated by four light-emitting diodes via a diffusor consisting of two opal-glass plates. The set of four light-emitting diodes was completely redundant, and the light-emitting diodes of one group were connected in such a way that, if one or more light-emitting diodes failed, the other ones would continue to emit light.

The frame was built up from three separate parts: the lower, middle, and top frames. The lower frame, connected to the focal-plane assembly platform by three flexible and adjustable feet, supported the middle frame and the connector bracket. The lower folding mirror was bonded to the bottom of the lower frame. The middle frame supported the star source and the top frame. The top frame was a bracket carrying the top folding mirror.

The main body and the mounting feet of the internal star pattern assembly were made from titanium. This metal was selected since its thermal expansion coefficient was sufficiently low to meet the stability requirement, while entailing a smaller mass penalty than that resulting from the use of invar. Pure titanium was used for the main body as this was more easily machinable. For the mounting feet, however, a titanium alloy TiAl6V4 was selected, as the greater strength allowed thinner blades, resulting in lower stresses in the focal-plane assembly platform. BK7 glass was used for the mirrors, as this had the same thermal expansion coefficient as titanium. The only part made out of invar was the star source housing, where a match with the much lower expansion of silica glass was required.

The optical block was made of Suprasil 1. It had a chromium layer coating with the star pattern at the front side of the optical block ($R = 1400$ mm), and an iraline coating at the rear side. The reflective coating consisted of three layers: chromium for adhesion, aluminium for reflection, and silica for protection.

The installation specification required provisions for shifting the internal star pattern assembly by 5 mm in three mutually perpendicular directions. Alignment devices between the flexible feet and the lower frame were used. As clamping by friction only was judged to be insufficient, shims were used throughout, even though this complicated the alignment. A further alignment possibility was provided by the rotation of the star source in the internal star pattern assembly frame. This was possible when the internal star pattern assembly was mounted on the focal-plane assembly platform.

Filters and Dichroics

In the chain of the image dissector tube relay optics, there was a switchable filter set, consisting of a chromaticity filter and a wide-band filter. There was a dichroic filter in the photomultiplier relay optics chain.

In order to calibrate the chromaticity of the payload in orbit (i.e. the geometrical shift in the grid coordinate position of stars of different colours—expected to be of the order of

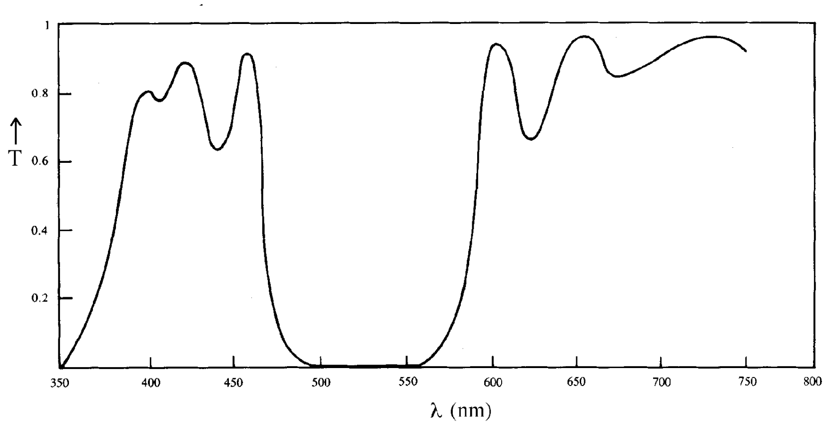

Figure 2.17. *Schematic transmission curve of the chromaticity calibration filter. The transmission characteristics of the filter resulted in two distinct images of each star, at two well-separated wavelengths, sufficient for the chromatically-induced displacements of the star images to be calibrated in orbit.*

1–2 milliarcsec, depending on star colour), a chromaticity filter was placed in the optical path.

The filter consisted of two wedges made of two different types of glass (PSK 53 and TiF 6), having the same refractive index at one wavelength, but different dispersions. The combination resulted in a plane-parallel, dispersing but non-deviating window. The two prisms, of 7°.5 angle, were 4 mm thick at mid-height, and were bonded together with SYLCO 14 cement, after a mirror coating of 90 nm spectral width around 520 nm was applied to the internal face of the PSK 53 glass. An anti-reflection coating in the range 350–800 nm was deposited on the external faces of the two prisms. The resulting transmission curve of the chromaticity calibration filter is shown in Figure 2.17.

The result is a double image of each star—a red and a blue image—on the image dissector tube, sufficiently displaced in the direction parallel to the slits to allow separate observation of the two images by the image dissector tube. This allowed the relative positions (via the modulation phases) of the two images of the star to be measured, and hence the chromaticity of the optical system.

In normal operations the chromaticity filter was not in the relay optics path. In order to compensate for the optical path length of the chromaticity filter, a wide-band filter was placed in the beam instead. The filter was made of 7.5 mm thick Suprasil 1 glass (to minimise 'darkening' caused by high-energy particle radiation in orbit), with an anti-reflection coating in the 350–800 nm range. Both the calibration filter and the wide-band filter had a face flatness of $\lambda/4$ peak-to-valley, and a face parallelism of better than 1 arcmin. The transmission curve of the wide-band filter is shown in Figure 2.18.

The dichroic filter, permanently present in the star mapper detection chain, had the effect of splitting the energy of the star mapper optical beam into two wavelength ranges, each range being directed to separate photomultiplier relay optics. Most of the light either went into the 'blue' photomultiplier channel (< 465 nm) by reflection, or to the 'visible' channel (> 475 nm) by transmission.

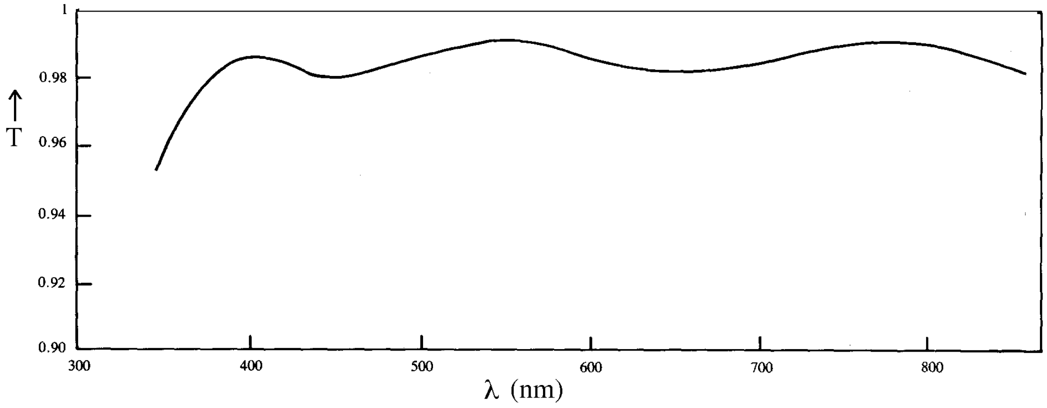

Figure 2.18. *Schematic transmission curve of the wide-band filter.*

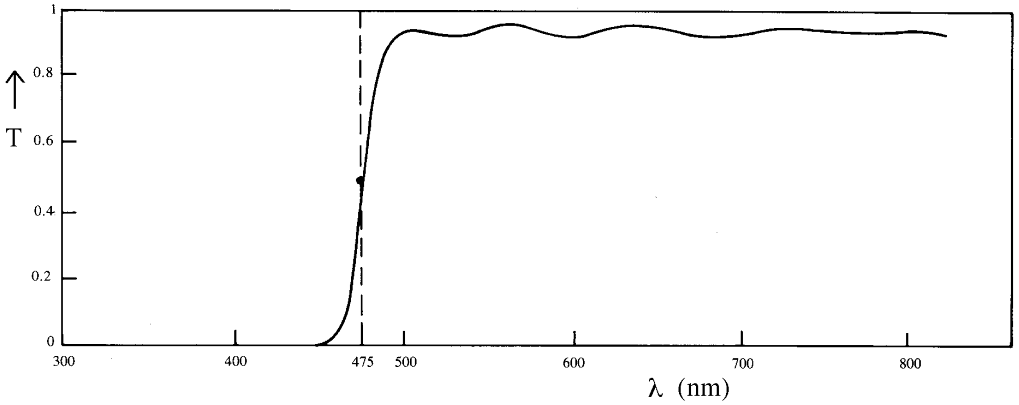

(a)

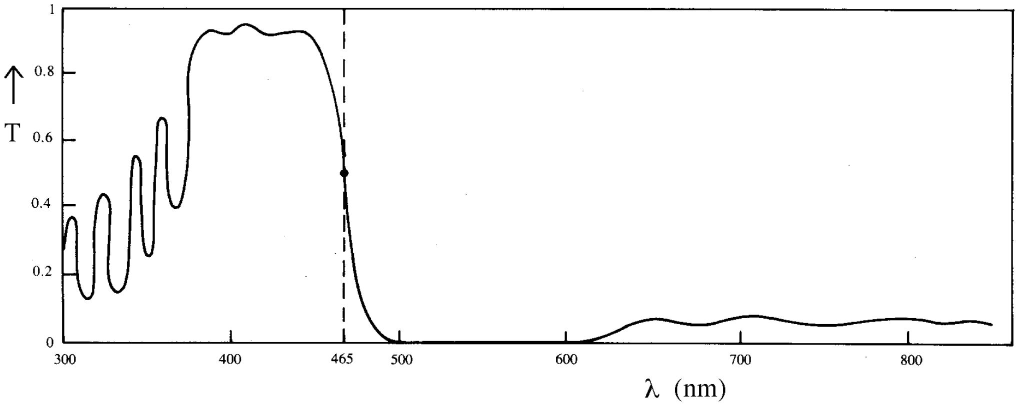

(b)

Figure 2.19. *Schematic transmission curves of the V_T (a), and B_T (b) star mapper channels.*

The dichroic filter was a coating deposited on 4-mm thick GG 475 glass. It worked at an incidence angle of 25°, where polarisation effects are limited. The 50 per cent point of this coating was at 465 nm in reflection and at approximately 475 nm in transmission. The second face of the dichroic filter was anti-reflection coated in the range 500–800 nm.

To increase the wavelength separation between the two parts of the spectrum, a blue filter was also included in the reflected path. This was a coating deposited on a 4-mm thick GG 375 Schott coloured glass window, giving zero transmission between 500–600 nm. An anti-reflection coating was applied to the second face in the range 350–500 nm. The dichroic coating and low-pass coating of the dichroic filter and blue filter were made of ZrO_2 and SiO_2, respectively, to get very hard layers, fully transparent as far as 300 nm. The flatness of the dichroic and blue filter face was $\lambda/2$ peak-to-valley. The resulting overall spectral transmission curves for the two channels are shown in Figures 2.19(a) and (b), (see also Table 2.3 and Table 2.4, which give the overall payload transmission, including the contribution of the dichroic filter).